

Title	A novel approach toward the integration of fully 3-D printed surface-mounted microwave ceramic filters
Authors	Fontana, Andrés;Delage, Anthony;Périgaud, Aurélien;Richard, Patrice;Carsenat, David;Acikalin, Guillaume;Verdeyme, Serge;Bonnet, Barbara;Carpentier, Ludovic;Delhote, Nicolas
Publication date	2023-05-16
Original Citation	Fontana, A., Delage, A., Périgaud, A., Richard, P., Carsenat, D., Acikalin, G., Verdeyme, S., Bonnet, B., Carpentier, L. and Delhote, N. (2023) 'A novel approach toward the integration of fully 3-D printed surface-mounted microwave ceramic filters', IEEE Transactions on Microwave Theory and Techniques. doi: 10.1109/TMTT.2023.3267541
Type of publication	Article (peer-reviewed)
Link to publisher's version	10.1109/tmtt.2023.3267541
Rights	© 2023, IEEE. Personal use of this material is permitted. Permission from IEEE must be obtained for all other uses, in any current or future media, including reprinting/republishing this material for advertising or promotional purposes, creating new collective works, for resale or redistribution to servers or lists, or reuse of any copyrighted component of this work in other works.
Download date	2025-08-02 23:05:43
Item downloaded from	<a href="https://hdl.handle.net/10468/14592">https://hdl.handle.net/10468/14592</a>



# UCC

**University College Cork, Ireland**  
Coláiste na hOllscoile Corcaigh

# A Novel Approach Toward the Integration of Fully 3-D Printed Surface-Mounted Microwave Ceramic Filters

Andrés Fontana<sup>1</sup>, Member, IEEE, Anthony Delage, Aurélien Périgaud<sup>2</sup>, Member, IEEE, Patrice Richard, David Carsenat, Guillaume Acikalin, Serge Verdeyme, Barbara Bonnet, Ludovic Carpentier, and Nicolas Delhote<sup>3</sup>, Member, IEEE

**Abstract**—A first approach toward the integration of heterogeneous electronic circuit technologies and fully 3-D printed ceramic microwave devices is discussed in this work. Additive manufacturing (AM) capabilities are explored for the development of multifunction surface-mount compact components used in different RF front-ends' scenarios. Monolithic ceramic bandpass filters (BPFs) are designed to operate in the X-Band and to assess the typical limitations of ceramic stereolithography (SLA) processes. A post-fabrication tuning method based on a laser engraving strategy is presented to overcome the manufacturing constraints and carry out the filters' correction. 2.5-D and 3-D printed four-pole filters were fabricated and tuned using the proposed methodology.

**Index Terms**—Additive manufacturing (AM), ceramic materials, microwave filters, stereolithography (SLA), surface-mount devices.

## I. INTRODUCTION

INITIALLY emerged as an innovative approach for fast prototyping, additive manufacturing (AM) technologies quickly became a viable alternative to some traditional manufacturing processes. AM can target a wide range of applications and domains [1], minimizing process wastes and reducing the production time thanks to the selective layer-by-layer fabrication. These features led to an exponential growth

Manuscript received 30 October 2022; revised 31 December 2022 and 31 January 2023; accepted 2 February 2023. This work was supported in part by Thales; in part by Thales Alenia Space, France; in part by the French Space Agency (CNES); and in part by the Région Nouvelle Aquitaine within the frame of the Désirh-3D Project. (Corresponding author: Andrés Fontana.)

Andrés Fontana was with the XLIM Laboratory, UMR 7252, University of Limoges, 87060 Limoges, France. He is now with the Tyndall National Institute and University College Cork, Cork, Ireland. (e-mail: afontana@ieee.org).

Aurélien Périgaud, Serge Verdeyme, and Nicolas Delhote are with the XLIM Laboratory, UMR 7252, University of Limoges, 87060 Limoges, France (e-mail: aurelien.perigaud@xlim.fr; serge.verdeyme@xlim.fr; nicolas.delhote@xlim.fr).

Anthony Delage is with the XLIM Laboratory, UMR 7252, University of Limoges, 87060 Limoges, France, and also with the Centre National d'Études Spatiales (CNES), 31400 Toulouse, France (e-mail: anthony.delage@xlim.fr).

Patrice Richard, David Carsenat, and Guillaume Acikalin are with Thales SIX GTS, 19100 Brive-la-Gaillarde, France (e-mail: patrice.richard@thalesgroup.com; david.carsenat@thalesgroup.com; guillaume.acikalin@thalesgroup.com).

Barbara Bonnet is with Thales Alenia Space, 31100 Toulouse, France (e-mail: barbara.bonnet@thalesaleniaspace.com).

Ludovic Carpentier is with the Centre National d'Études Spatiales (CNES), 31400 Toulouse, France (e-mail: ludovic.carpentier@cnes.fr).

Color versions of one or more figures in this article are available at <https://doi.org/10.1109/TMTT.2023.3267541>.

Digital Object Identifier 10.1109/TMTT.2023.3267541

of the technology in the automotive, aerospace, and medical industry sectors, among others [2].

In recent years, the increasingly demand of microwave devices as a result of the popularization of modern wireless communication systems encouraged the exploration of new ways to conceive electronic components. The implementation of massive multiple-input multiple-output (MIMO) beamforming systems in 5G communications [3], [4], Internet of Things (IoT) applications [5], [6], and the deployment of nanosatellite constellations [7] demands cost-effective highly integrated hardware solutions [8]. Different perspectives were investigated to fulfill these requirements leveraging the continuous advancements in 3-D printing technologies [9]. The possibility of performing complex geometrical structures in one single part expands the manufacturing flexibility, simplifies the assembly methods, and encourages the emergence of innovative solutions. The high versatility of available materials in addition to the enhanced fabrication accuracy in modern 3-D printers motivated the utilization of AM for the conception of microwave devices before unthinkable [1], [10]. Exceptional work has been done in this regard to successfully implement 3-D printing technology in microwave applications. Several multifunction (electrical, thermal or structural) designs were developed leading to miniaturized and lighter components. Monolithic bandpass filters (BPFs) [11], orthomode transducers [12], directional couplers [13], and horn antennas [14] are some examples of microwave devices reported using ceramic and photopolymer stereolithography (SLA), and selective laser melting (metals) processes [15], [16]. Inkjet and Aerosol Jet Printing technologies were also used for printed electronics such as interconnection lines and planar circuits on flat flexible substrates and 3-D surfaces [17], [18], [19]. There is a particular interest to integrate heterogeneous technologies in printed circuit boards (PCBs) and provide novel functionalities or improved features at subsystem level. Some efforts were made to fabricate 3-D printed multichip modules (MCMs) and the integration of embedded devices [20]. These modules might be directly printed together with the PCB or assembled onto a carrier substrate using surface mount technology (SMT) [21].

Ceramic-based devices are an interesting alternative for hyper-frequency applications, thanks to their good electromagnetic properties, such as low loss tangent.

Particularly, ceramic devices can be implemented in microwave bands where good performances and compact dimensions are required. Miniaturized microwave filters with relatively good quality factor and temperature stability can be developed with low-loss ceramics. Ceramic resins such as alumina and zirconia are currently commercially available for SLA process [22]. Even though, the current ceramic SLA printing resolution permits the fabrication of better-defined structures, manufacturing tolerances are still a critical constraint that limit the operating frequency of complex microwave devices.

Laser techniques are currently a well-established industry standard used to complement or replace manufacturing processes such as surface treatment, drilling, and cutting. This approach stands out for their good accuracy and low manufacturing dispersion, and can be applied to a great variety of materials ranging from metals, polymers, and ceramics. Solid-state lasers based on crystals such as yttrium aluminum garnet ( $Y_3Al_5O_{12}$ ) or YAG became popular in the 1960 s [23]. Nd-YAG lasers emit light waves with high energy at the near infrared region and can cut high reflecting materials such as aluminum or copper. Trimming techniques have been used in post-fabrication tuning of SMD resistors [24] and planar microwave filter correction [25], and served as inspiration in this work for the software-assisted post-fabrication tuning of 3-D printed cavity filters.

Most of the designs reported in the literature implement ceramic SLA for the construction of monoblock components in a 2-D/2.5-D-fashion [11], [26]. However, the development of fully 3-D SMD ceramic components and their integration with heterogeneous technologies has not been widely investigated. Additively manufactured microwave components could be designed to provide several useful functionalities and adapt them to the PCB layout to: facilitate the board floor planning and routing; isolate electromagnetically specific regions; integrate disparate technologies and functionalities in the same space; and reduce the interconnection paths (see Fig. 1). This approach can be useful in applications such as modern telecommunication systems, where the area is usually a constraint and a good trade-off between technology integration,  $Q$ -factor, and temperature stability is desired. These features can be particularly exploited in RF front-ends to simplify the board layout, improve the system performances, and enhance the system integration. LEO/MEO satellite non-terrestrial networks (NTN) [27], [28], nanosatellite payloads [7], defense applications and unmanned aerial vehicles (UAV) [27], [29], and 5G MIMO beamforming transceivers [30] might benefit from these concepts.

In this work, the development of 3-D ceramic-filled cavity filters is explored to determine the current manufacturing limitations found during the realization of the different scenarios proposed in Fig. 1. A tuning method based on a principle given in [25] is introduced for the correction of the state-of-the-art monolithic SLA components. The method implements the laser engraving of specific planar patterns on the filter metal coating to perform the correction of the resonant frequency ( $f_0$ ) and the inter-resonator coupling. The procedure is first tested on 3-D printed 2.5-D filters at 8 GHz

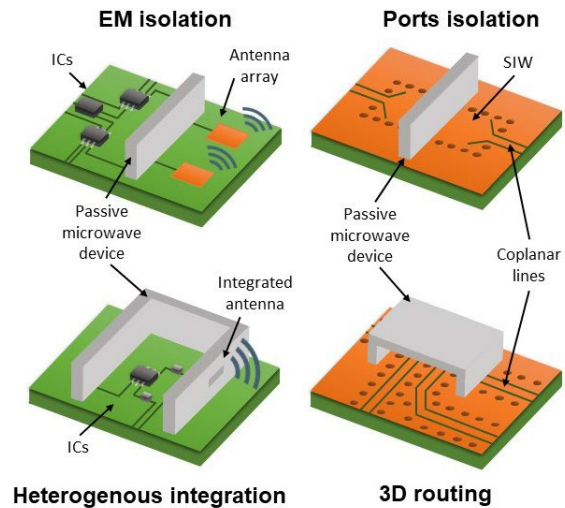


Fig. 1. AM ceramic devices adapted to different scenarios.

to validate the methodology. Four SMD 3-D printed BPF prototypes are then designed, fabricated, and corrected to test the method and overcome the manufacturing imperfections. Additionally, a transition for the interconnection of coplanar lines to  $TE_{101}$  rectangular cavity resonators is discussed. The obtained results are intended to provide useful information toward the future implementation of complex subsystems embedded in 3-D ceramic microwave devices.

## II. LASER ABLATION TECHNIQUE FOR MONOLITHIC BPFs CORRECTION

Many methods have been proposed in the literature to compensate the lack of perfect manufacturing accuracy. Tuning screws are often used in metal and plastic air-filled cavity devices to disturb the electromagnetic field inside the devices [13]. Movable parts are also used to modify the inner dimensions of resonators [31]. The optimal position of the tuning screws or movable parts in every cavity is calculated with the support of specialized algorithms [32], [33], [34], [35]. However, these approaches cannot be well adapted to monolithic ceramic-filled cavity filters [36]. Specific methods were proposed to adjust the frequency response of such components during a post-fabrication step. The engraving of planar patterns on the device surface was used in [37] to finely tune the resonant frequency of substrate-integrated waveguide (SIW) hybrid planar waveguide resonators (HPWRs) by manually disconnecting tuning elements through wirebonds. A similar technique was applied in [38] where a ten-pole monoblock dielectric filter was finely tuned by scratching the metal surface at strategic spots. In [39], laser ablation was used to correct the frequency response by selectively piercing the metal layer of planar filters. Cross open-loop resonators were tuned using presimulated abacus to adjust the center frequency. Nonetheless, this procedure does not take into account the side-effect of the correction in the rest of the coupling factors, leading to an incomplete estimation of the filter response adjustment.

The etching of tuning patterns is an irreversible technique, useful to compensate the fabrication error in microwave

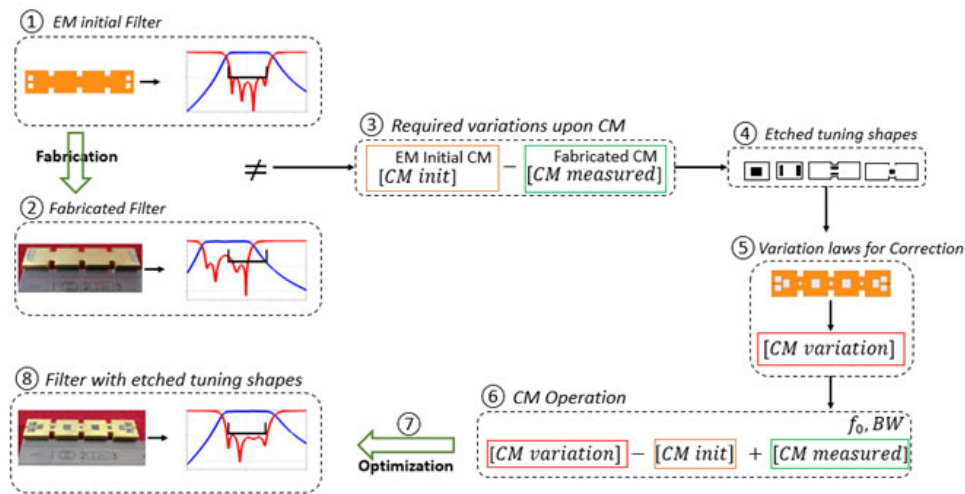


Fig. 2. Post-fabrication tuning method process flow.

devices. A method based on the coupling matrix (CM) theory [40], and valid for any filter with unique CM representation, is introduced in this work by laser engraving planar patterns on the device conductive surface. This method can be applied to single- or multimode resonators regardless the filter technology. Filters based on noncoupled resonator are out of the scope of this method. The proposed patterns provide the necessary effect to modify the resonant frequency and inter-resonator coupling. The method estimates the relationship between the patterns' layout parameters and their impact on the frequency response to carry out the correction of monolithic ceramic-filled cavity filters. The variations of every coupling factor produced as a product of the patterns dimension modification is contemplated in this approach to enhance the process accuracy.

Fig. 2 depicts the complete tuning process flow of a generic filter corrected with the proposed method.

- Step ①: Definition of specifications such as center frequency and bandwidth. Design and EM simulation of the device (EM initial filter).
- Step ②: Fabrication and measurement of the device. A post-fabrication tuning step is needed if the filter response does not satisfy the initial specifications owing to the manufacturing dispersion.
- Step ③: CM extraction from the initial and measured filter. All the couplings' factors, including the parasitics, are extracted during the procedure. Both matrices are subtracted to determine the difference between each parameter.
- Step ④: Identification of the tuning patterns needed according to the calculated coupling offset and the corrections required (see Section III-B).
- Step ⑤: The tuning patterns are included in the initial filter design to simulate their EM effect. At the beginning, the initial dimensions of the patterns ( $x_o$ ) are not necessarily optimized. Therefore, the EM variation laws for each pattern are needed to determine their final size. A set of matrices is extracted for each tuning pattern

variation (dimensions and position). The variations are simulated separately to extract the corresponding CM of the filter, obtaining their EM influence on all the matrix coefficients, simultaneously. For instance, to obtain the influence of the size variation  $\Delta x$  of a tuning pattern on a fourth-order filter, two EM simulations ( $x_o \pm \Delta x$ ) are conducted. All the coefficients of the coupling matrices are extracted, revealing the impact of the size variation not only on the target resonator, but also on the overall filter structure. This process is conducted for all the geometrical parameters of every pattern added to the filter.

- Step ⑥: To isolate the tuning patterns dimensions effect, the fabricated filter response is linked to the patterns size by subtracting the initial CM to the CM extracted for each variation in Step ⑤. The results are added to the fabricated filter CM allowing to optimize the final shape. Each CM is normalized according to the center frequency and bandwidth of the initial specifications.
- Step ⑦: The  $S$ -parameters of the tuned component can be obtained by analytical calculation from the CM. The frequency response is compared to the bandwidth and center frequency goals. The inputs used in this step are the geometrical variations of the tuning patterns which are optimized until the fulfillment of the goals by classical optimization algorithms [41]. At the end, the final geometrical dimensions are obtained as outputs of the process and applied to the tuning patterns in the EM simulation software.
- Step ⑧: As a result of Step ⑦, a filter response closer to the initial requirements should be obtained. The patterns are applied to the fabricated filter and remeasured. Nevertheless, more than one iteration may be necessary to finely tune the device and meet the final specifications. In this case, the new filter response is used as input in Step ② to restart the tuning process. Special attention must be taken to avoid excessive material over-etching to prevent an unexpected frequency shift.

TABLE I

DIFFERENT COPLANAR TUNING PATTERNS CASE OF STUDY FOR THE CORRECTION OF DIELECTRIC-FILLED CAVITIES FREQUENCY (TOP) AND THEIR COUPLING (BOTTOM)

Tuning pattern	Main effect
 Square slot (SS)	Frequency $\uparrow$ as area $\uparrow$
 Rectangular slot (RS)	Frequency $\downarrow$ as length $\uparrow$
 Square slot (SS)	Coupling $\downarrow$ as area $\uparrow$
 2 Rectangular slots (2-RS)	Coupling $\uparrow$ as length $\uparrow$

### III. TUNING METHOD APPLIED TO 3-D PRINTED FILTERS

#### A. Fabrication Process of Monolithic Ceramic Filters

Several 2.5-D monoblock Alumina cavity filters and resonators were printed as devices under test (DUTs) with ceramic SLA to experimentally test the tuning approach. The SLA process consists of the layer-by-layer curing of a photo-sensitive liquid resin filled with ceramic particles [42]. Each layer of resin is selectively polymerized by an UV laser beam controlled by a dual-axis ( $XY$ ) mirror galvanometer to create the 3-D structure. The ceramic parts are cleaned with solvents to remove possible rests of resin and subjected to a debinding and sintering process in a furnace to evaporate the solvents and harden the structure. Depending on the material the parts can be heated up to 1600 °C. The low-loss ceramic material chosen for these tests presented electromagnetic properties of  $\epsilon_r = 9.94$  and  $\tan \delta = 6.10^{-4}$ .

In regard to the samples coating, metal plating processes such as electroless (copper), electroplating (copper, gold) or chemical vapor deposition (CVD) are compatible solutions with ceramic technologies [43]. Electroless copper was applied in this first fabrication batch owing to the simplicity of the method and its capability to homogeneously coat complex 3-D objects.

The manufactured DUTs were exposed to this process and covered with 3–4  $\mu\text{m}$  thick conductive layer. An extra layer was also deposited with gold electrolysis as a protection to prevent oxidation. An electrical conductivity between 16 and 20  $\text{S}/\mu\text{m}$  was measured (bulk copper conductivity equals to 58  $\text{S}/\mu\text{m}$ ) in the metallized devices by implementing the resonant cavity technique [43] up to 28 GHz.

#### B. Study of Planar Tuning Patterns

The manufactured DUTs were designed to operate using the  $\text{TE}_{101}$  mode at 8 GHz. To tune the filter resonant frequency and inter-resonator couplings, specific patterns have to be etched on the metal enclosure of each resonator and inductive iris. Table I depicts the two tuning layouts studied to interact with the fundamental resonant mode of the cavity: a square

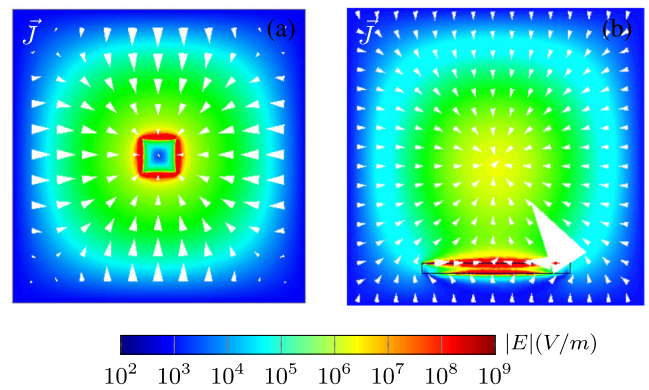


Fig. 3.  $E$ -field distribution and current density vector field ( $\vec{J}$ ) plots for (a) centered SS ( $x = 4$  mm) and (b) sided RS ( $x = 4$  mm and  $y = 0.28$  mm) placed on the top face of a ceramic-filled resonator ( $8 \times 8 \times 2$  mm).

slot (SS) and rectangular slot (RS) pattern. These shapes were chosen owing to their fabrication simplicity and low accuracy required. The areas colored in blue represent the laser engraved region where the metal layer is lifted. Over-etching effects were not taken into account in this analysis and the total thickness of the dielectric filter is considered unmodified along the process. A full-wave EM simulator software (Ansys HFSS<sup>1</sup>) was utilized to conduct the simulations and estimate the patterns effect on the DUTs operation. On the one hand, the frequency shift of the resonant mode ( $\Delta f_0$ ) was analyzed using  $8 \times 8 \times 3$  mm square resonators. The pretuned unloaded quality factor measured in the samples was  $Q_o = 760$ . On the other hand, the patterns linked to the inter-resonator coupling variation were simulated in a  $8 \times 18.5 \times 3$  mm two-pole filter as shown in Table I.

The etched slots cause a modification in the device boundary conditions when centered in the middle of the cavity top face. An imperfect magnetic wall is added in a region of maximum  $E$ -field as a result of the permittivity difference between the air/ceramic interface [44]. Starting from a RS with a fixed length ( $x$ ), the effect is increased as the width ( $y$ ), and therefore the aperture surface, is increased until reaching the SS pattern. The equivalent  $\text{TE}_{101}$  mode is reduced as the boundary conditions change, driving to an increase of  $f_0$  for the same cavity size [44]. Fig. 3(a) depicts the  $E$ -field distribution for this case. If the centered patterns are shifted from the middle to the cavity edge, the current density ( $\vec{J}$ ) on the metal plate surface augments owing to the maximum magnetic field distribution located on the borders. The perpendicular direction of  $\vec{J}$  with respect to the slot [see Fig. 3(b)] polarizes the aperture as the distance from the edge is reduced making it function as a slot antenna [45]. Waveguide and SIW RS antenna arrays have been widely reported in the bibliography [46], [47]. The impact of the antenna coupled to the cavity results in a deformation of the  $E$ -field that can be understood as an added capacitive effect decreasing the resonant frequency of the mode as the slot length is increased.

<sup>1</sup>Registered trademark.

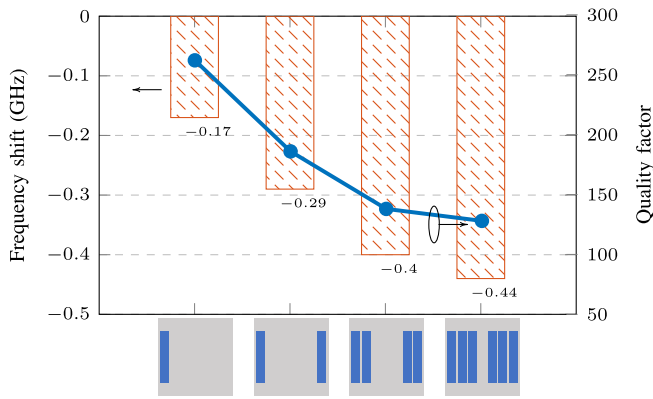


Fig. 4. Simulated  $\Delta f_0$  and  $Q_o$  for several in-parallel RS patterns ( $x = 4$  mm and  $y = 0.28$  mm).

The slot width size for these cases is considered to be much less than the resonant frequency of the antenna ( $y \ll \lambda_{RS}$ ).

Effectively, EM simulations showed a frequency shift effect to higher frequencies when placing the square and RS patterns in the center of the resonator. The resonant cavity seems to be more sensitive to the centered SS than to the RS pattern. A  $\Delta f_0 = +710$  MHz was observed in the first case for a pattern dimension of  $x = 4$  mm in expense of a  $Q_o$  reduction of 38%. On the contrary, an offset of  $\Delta f_0 = +10$  MHz with a negligible  $Q$ -factor degradation was found for a RS pattern with size  $x = 4$  mm and  $y = 0.28$  mm. However, the RS pattern proved to be a more efficient solution to shift the resonance to lower frequencies. The frequency shift sensitivity in this case was increased for the RS and decreased for SS pattern when the layouts were shifted toward the cavity edges. Results showed a  $\Delta f_0(\text{RS}) = -170$  MHz ( $\Delta Q_o(\text{RS}) = -66\% Q_o$ ) and  $\Delta f_0(\text{SS}) = +22$  MHz for patterns separated  $90 \mu\text{m}$  from the resonator edge. Fig. 4 illustrates the simulated RS pattern effect on the frequency shift ( $\Delta f_0$ ) and  $Q$ -factor ( $Q_o$ ). Furthermore, several in-parallel RS patterns were also tested on each side to boost the frequency shift effect. The patterns were designed for simulation tests using the same dimensions as in the prior layouts and separated  $230 \mu\text{m}$  between them. The frequency shift and  $Q$ -factor evolution were analyzed for designs implementing from 2 to 6 in-parallel RS patterns. The frequency shift range obtained with one RS pattern is enhanced by 170%, 235%, and 258% when using two, four, and six elements. For instance, an offset of  $-290$  MHz can be obtained with two-parallel RSs. The quality factor is reduced around an extra 10% in this case ( $-76\%$  of the initial  $Q_o$ ).

The same principle can be applied to control the inter-resonator coupling factor ( $k$ ) in inductive irises. Similar simulations were carried out to estimate the effect of the patterns. In this case, the utilization of different layouts and positions on top of the iris directly affects the  $E$ -field even and odd resonance modes of the structure [48], [49]. As illustrated in Fig. 5(a), the implementation of two-RS patterns located at  $230 \mu\text{m}$  from the iris edge ( $y = 280 \mu\text{m}$ ) shifts the even mode to lower frequencies. However, the odd mode remains almost unaffected for this case. This is a consequence

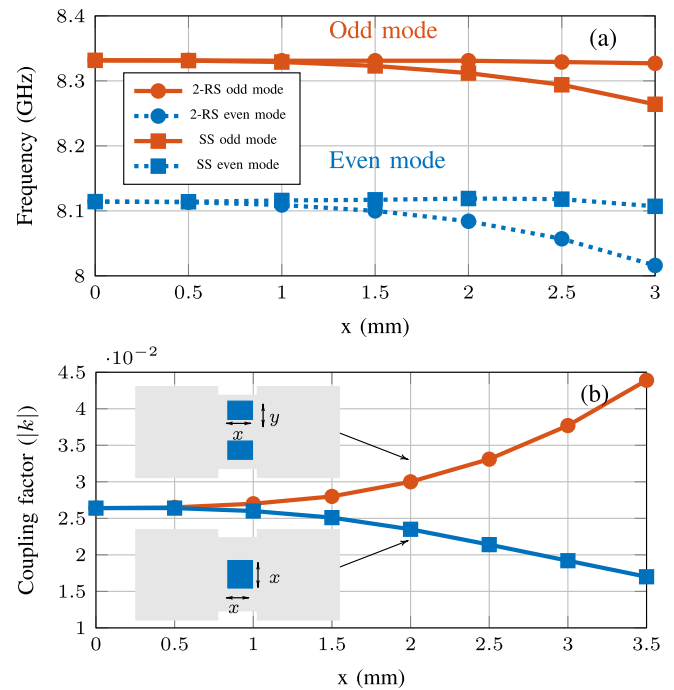


Fig. 5. (a) Simulated even and odd mode frequency and (b) inter-resonator coupling factor variation provided by SS and 2-RS tuning layouts.

of the current density distribution in both resonant modes that polarizes the slots only for the first example. Therefore, the coupling factor calculated as expressed in the following equation augments as the slot length increases:

$$|k| = \left| \frac{f_e^2 - f_o^2}{f_e^2 + f_o^2} \right|. \quad (1)$$

Similarly, when the patterns are located in the center of the iris the current density only excites the slot in the odd mode, shifting the resonant frequency to lower values [see Fig. 5(a)]. Hence, as shown in Fig. 5(b), the effect of this position results in a decrease of the coupling factor.

The SS and RS tuning patterns analyzed in each case seem to be a balanced solution for their application in the monoblock ceramic filters tuning method proposed. The chosen patterns can increase or decrease the resonant frequency and the coupling factor between adjacent resonators. According to simulation results, the implementation of both patterns can offer a frequency shift capability of about  $+9\%$ – $-15\%$  and a coupling tuning range of  $+66\%$ – $-35\%$ , respectively.

### C. Experimental Implementation of Tuning Patterns

Experimental tests were conducted to corroborate the simulated effect of the tuning patterns on 3-D printed Alumina cavity resonators (see Fig. 6) and two-pole filters (see Fig. 7). The layouts engraving was performed with a  $50 \mu\text{m}$  diameter laser beam ( $\lambda = 1064$  nm) and the devices measured with a ZVA 87 VNA and  $250 \mu\text{m}$  pitch GSG probes. The tests conducted in single cavity resonators are depicted in Fig. 6. Measurements are in good agreement with the simulated tuning behavior expected from both patterns. Discrepancies between experimental and simulated results seem to be a

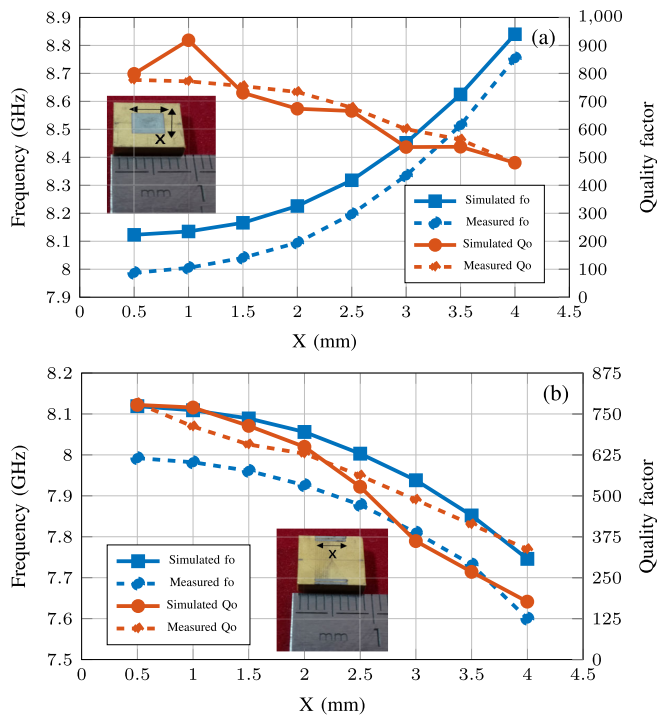


Fig. 6. Measured and simulated (a) SS and (b) 2-RS patterns  $\Delta f_0$  and  $Q_0$  applied to 3-D printed Alumina resonators.

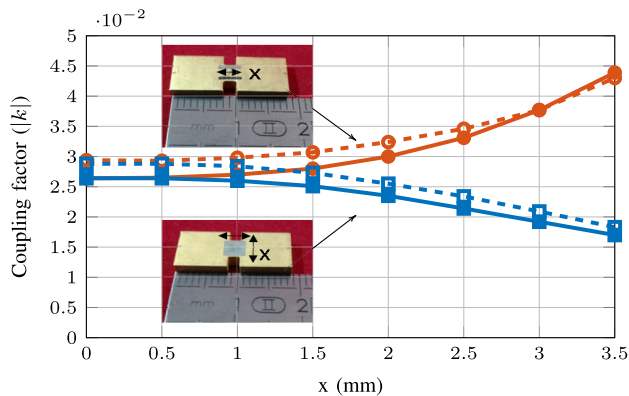


Fig. 7. Comparison of simulated (solid lines) and measured (dashed lines) coupling factor tuning effect.

consequence of the non-homogeneous metallization thickness and laser machining accuracy. Nonetheless, these differences do not represent a critical issue since the method implements the relative variation of  $\Delta f_0$  and  $k$  for the filter tuning. Quality factor measurements reveal a decreasing trend in both examples as the slot length  $x$  increases, leading to a  $Q$ -factor degradation between 35% and 57% of the initial value. Experimental tests exhibit the same trade-off observed in simulations between  $\Delta f_0$  and the radiation losses introduced by the metal enclosure openings.

The inter-resonator coupling evolution is plotted in Fig. 7 as a function of the SS and two-RS length. The even and odd mode analysis [48] was used to experimentally assess the coupling coefficients by measuring the resonant frequencies of the modes as a function of the slots' dimension. The coupling factor behavior of the two-pole filter fabricated exhibits

a good agreement with simulations. The experimental tests confirm the capability of the selected patterns to increase and decrease the coupling factor of two resonators linked by an inductive iris.

#### IV. POST-FABRICATION TUNING EVALUATION

The results obtained during the experimental tests revealed a relative variation of the frequency shift and the coupling law close to those estimated in simulations for all the tuning shapes. Therefore, the chosen patterns demonstrated to provide the EM effect needed for their utilization in the post-fabrication tuning method exposed in Section II. However, an application example is required to corroborate the proper functioning of the overall methodology before their implementation in complex structures. Two four-pole Chebyshev filters were fabricated, characterized, and tuned to compensate the SLA manufacturing dispersion and comply with the initial specifications.

##### A. Post-Fabrication Tuning Setup

A specific setup was prepared to carry out the correction of 3-D printed ceramic filters and monitor in real time the effect of the laser machining on the frequency response. The main purpose of the setup depicted in Fig. 8 was to reduce the process time and potential inaccuracy issues driven by the continuous sample manipulation and realignment through several work stations. The implementation of the laser machine facilitates the engraving of complex shapes in difficult access areas while maintaining the integrity of the sample. The metallized samples are placed inside the laser machine chamber and released once the DUTs meet the specifications.

The laser machine consists of a main engraving chamber and an aspiration device. The laser head is located inside the engraving chamber, as well as a moving plate where the sample is deposited. The platform can be manually operated along the  $x$ - and  $y$ -axes or automatically displaced to three pre-programmed positions (1–3) as marked in Fig. 8(b). The position 1 regroups the laser and a camera to control the alignment of the etched patterns. Movement along the  $z$ -axis is also possible, allowing the machining of 3-D objects. The position 2 counts with a high-resolution camera coupled to the first one to check the quality of the engraved patterns. The position 3 functions as a measurement area to obtain the  $S$ -parameters. This space is equipped with a custom probe station externally connected to a VNA [see Fig. 8(a) and (b)] and a third camera to facilitate the alignment with the DUTs coplanar ports. The measurements are always conducted in the  $xy$  plane to avoid rotating the probe tips. In the case of the 2.5-D filters, the tips are placed on the engraved coplanar accesses [see Fig. 8(c)], while the 3-D filters measurements (see Section VI) are carried out at the ports placed on the carrier board. Prior to the characterization and tuning process, the VNA is calibrated in the GSG probes interface with a two-port TOSM procedure. The whole setup is handled by an external computer and screens to visualize the different process steps.

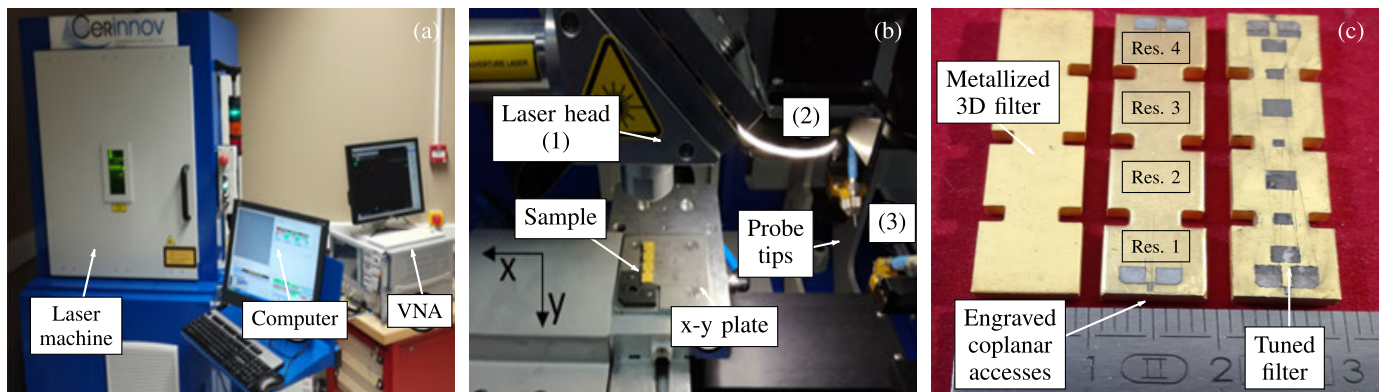


Fig. 8. Post-fabrication device tuning work station: (a) measurement instruments and machines setup, (b) laser machine chamber arrangement, and (c) laser engraving procedure of the samples. 1: The plate position for the laser etching, 2: the engraving verification with a high-resolution camera, and 3: the probe station position for electrical measurements.

The post-fabrication tuning method introduced in Section II is implemented on the testbench as follows.

- 1) Step ②: The manufactured filter is measured in position 3.
- 2) Step ⑧: Once the tuning patterns are estimated (manually or automatically) using the extracted data from the VNA, the  $xy$  plate is displaced to position 1. The patterns are then engraved using the generated CAD files. A laser machining quality check is performed in position 2 and the filter is remeasured in position 3. A second loop can be launched if the results do not comply with the specifications.

### B. BPF Test

A classical inline topology was implemented in two fourth-order Chebyshev filter samples. The parts were fabricated using the same process as explained in Section III. Fig. 8(c), illustrates the three stages by which the samples are exposed during the fabrication (stage 1 and 2) and post-fabrication step (stage 3). The BPF were designed to provide a center frequency of 8 GHz, an equiripple bandwidth of 0.3 GHz and 20 dB of return loss. The filter ports are laser etched during the second stage on top of resonators 1 and 4. The  $S$ -parameters of the device are measured after the port engraving and used as input in Step ② of the tuning method if the specifications are not satisfactory.

Considering the results observed in Section III-C, a limited tuning range can be practically applied. The capability to tune a given fabricated filter back to its initial specifications results in a  $+9\%/ -15\%$   $f_0$  and an inter-resonator coupling variation of  $+66\%/ -35\%$ . The tuning range allows to evaluate the correction of the measured frequency response beforehand. The tuning process is aimed to perform the necessary corrections in only one iteration with one unique pattern per resonator/coupling filter element. However, a second loop can be carried out to compensate the own dispersion of the laser, and even two different patterns can be combined in the same filter element (e.g., SS and RS slots in the same resonator) to achieve a fine tuning. Furthermore, the selection of the required tuning patterns and their corresponding size in each part of the measured pretuned device can be automated

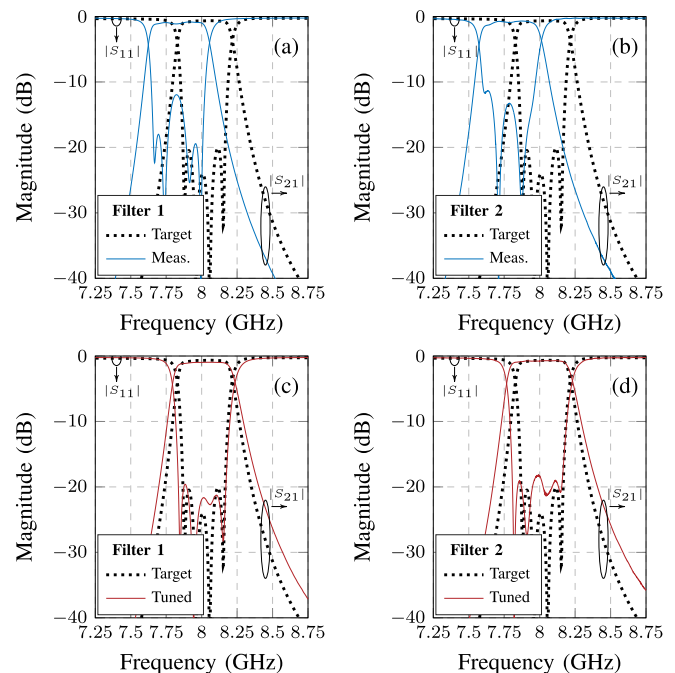


Fig. 9. Post-fabricated and tuned  $S$ -parameters measurements of two 3-D printed four-pole filter samples. Simulated design and pre-tuning manufactured results of (a) sample 1 and (b) sample 2. Simulated design and measured results after tuning process of (c) sample 1 and (d) sample 2.

with the use of software-assisted tools. EM solvers can be interfaced with programming languages such as Python or Visual Basic to perform the patterns sensitivity analysis on the measured structure (Steps 4–7 in Fig. 2). Such solution is out of the scope of this article. However, its implementation is straightforward, it can be implemented in highly automatized industry processes and help to reduce the fabrication time and costs, avoiding expensive redesign and refabrication stages. Fig. 9(a) and (b) depicts the DUTs simulated and measured  $S$ -parameters used as the tuning method inputs (Step ③). Results show a center frequency offset of  $f_{0\text{filter1}} = 0.18$  GHz (2.25%) and  $f_{0\text{filter2}} = 0.22$  GHz (2.75%), and return loss of  $-12$  and  $-11.4$  dB, respectively. The frequency shift is well within the available tuning range, allowing in theory the device correction. Fig. 9(c) and (d) exhibits the final results obtained after one loop completion of the method. As it can

TABLE II  
SIMULATED AND MEASURED  $S$ -PARAMETERS BEFORE AND AFTER THE  
POST-FABRICATION TUNING FOR TWO FILTER SAMPLES

Sample	$f_0$ (GHz)	BW (GHz)	IL (dB)	RL (dB)	Flatness (dB)	$Q_0^*$
Simulated filter	8.00	0.30	0.7	20	0.03	800
Meas. filter 1 (pre-tuning)	7.82	0.37	0.83	12	0.2	730
Meas. filter 1 (post-tuning)	8.00	0.33	0.96	19.61	0.02	537
Meas. filter 2 (pre-tuning)	7.79	0.36	0.72	11.36	0.17	800
Meas. filter 2 (post-tuning)	7.98	0.35	0.75	18.25	0.05	690

\* Effective quality factor estimated from an equivalent 4th order Chebyshev band-pass filter with the same  $f_0$  and bandwidth.

be seen, the implementation of the tuning process enhanced the filter response bringing it back to the initial specifications. The maximum bandwidth correction achieved was 40 MHz instead of the 60 and 70 MHz originally targeted. The equivalent unloaded  $Q$ -factor extracted before and after the corrections was 730 and 537 for the first sample, representing a degradation of 26%. In the case of the second sample, the extracted  $Q$ -factor was 690% or 14% less with respect to the pretuned value. Comparisons between the corrected filters and the quality factor variation exhibit slightly less losses in the case of filters than in resonators. A summary of the filters parameters is given in Table II. Differences between simulations and measurements in both filter samples are due to the laser over-etching ( $<10 \mu\text{m}$ ).

The experimental corroboration of the laser tuning method capability to evaluate and compensate the effect of manufacturing inaccuracies in 3-D printed microwave cavity filters was the fundamental milestone for the development of more geometrically complex arrangements.

## V. SURFACE-MOUNTED 3-D PRINTED CERAMIC FILTERS

The implementation of folded ceramic structures fabricated with AM techniques can be potentially adapted to the different scenarios introduced in Fig. 1. Moreover, a great variety of filter configurations could be easily developed by leveraging the 3-D interconnection of resonators in the space. Even though a good trade-off between ceramic SLA fabrication tolerances and miniaturization can be achieved, the complexity of the structures can rapidly spoil the filter response. To address these constraints, several arrangements of the same topology were investigated using the fabrication process and the tuning method implemented in the previous 2.5-D filters. First steps toward the design, characterization, and fabrication of SMD ceramic folded filters are presented below.

### A. I/O Terminal Structure Analysis

The excitation of ceramic-filled cavity resonators is generally performed with coplanar accesses in horizontally oriented structures [50]. However, this configuration limits the advantages of 3-D devices.  $TE_{101}$  mode rectangular cavity resonators exhibit a symmetric distribution of the EM field

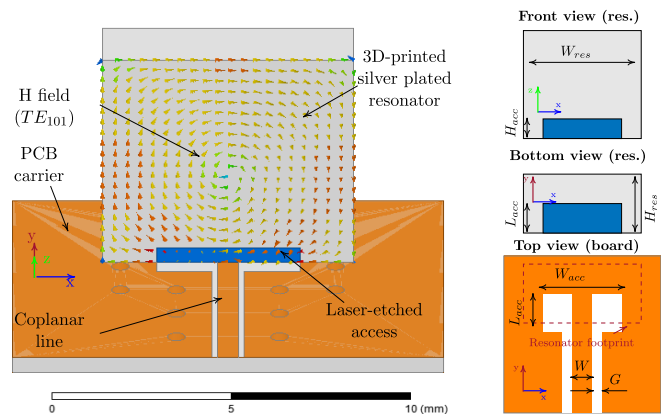


Fig. 10. Coplanar to  $TE_{101}$  cavity resonator transition: magnetic field and surface-mount assembly.

with maximum  $H$ -field distribution located on the sides. The  $H$ -field distribution can be used for the development of MC transitions by flipping the resonator sideways. Thanks to the symmetry of the field, the structure can be rotated and placed on any side using every time the same configuration. Proper transitions are needed to perform the assembly between the interconnection lines and the ceramic filter terminal ports. A magnetically coupled excitation is proposed in Fig. 10 for a rectangular resonator with  $L_{\text{res}} = W_{\text{res}} = 7 \text{ mm}$  and  $H_{\text{res}} = 2 \text{ mm}$ . The transition is composed of a  $50 \Omega$  CPWG line ( $G = 169 \mu\text{m}$  and  $W = 610 \mu\text{m}$ ) terminated in a short circuit to provide maximum magnetic field below the ceramic resonator. The line gap is enlarged to boost the magnetic field radiation in the nearby area. When using this approach, the radiated magnetic field partially matches with the  $TE_{101}$   $H$ -field distribution in the resonator/board interface. A rectangular aperture is opened on the metallic coating of the ceramic resonator to propagate the radiated field into the device. Both, the access and the CPWG line are centered with respect to the structure. The external coupling  $Q_{e_o}$  can be controlled by changing the access length ( $L_{\text{acc}}$ ), width ( $W_{\text{acc}}$ ) and height ( $H_{\text{acc}}$ ) [see Figs. 10 and 11(a)].

Despite no particular actions should be taken to avoid short circuits during the assembly, the component misalignment could affect the coupling  $Q_{e_o}$  between the coplanar line termination and the resonator access. A statistical analysis was performed to assess the misalignment impact when utilizing industrial pick and place setups. The study was carried out using resonators with access dimensions of  $W_{\text{acc}} = 4 \text{ mm}$ ,  $L_{\text{acc}} = 1.1 \text{ mm}$ , and  $H_{\text{acc}} = 0.2 \text{ mm}$ . The external coupling simulated for these dimensions was  $Q_{e_o} = 38.5$ . A placement uncertainty in  $x$ -,  $y$ - and  $\theta$  was considered and described by a normal distribution with deviations of  $\Delta x|_{\pm 6\sigma} = \Delta y|_{\pm 6\sigma} = \pm 80 \mu\text{m}$  and  $\Delta \theta|_{\pm 6\sigma} = \pm 0.01^\circ$  [see Fig. 11(b)]. A Gaussian distribution fit of the statistical analysis reveals a  $Q_{e_o} = 38.51 \pm 0.19$ , representing a variation of  $|S_{11}(\text{dB})| = \pm 1 \text{ dB}$  and  $|S_{21}(\text{dB})| = \pm 0.01 \text{ dB}$  within the reference filter passband presented below.

### B. BPF Design

The MC rectangular cavity resonators were implemented in the different 3-D-printed filter prototypes illustrated in

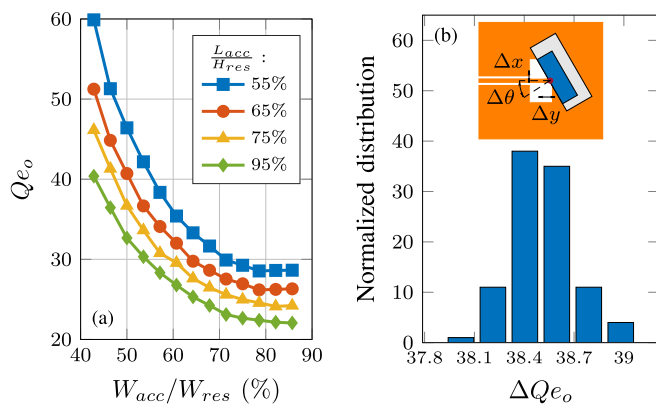


Fig. 11. I/O terminal external quality factor analysis: (a) dependency with geometrical dimensions ( $H_{acc} = 0.2$  mm) and (b) variability due to misalignment.

Fig. 12. Several four-pole Chebyshev BPFs were conceived for their fabrication in low-loss Alumina ( $\epsilon_r = 9.15$ ,  $\tan \delta < 10^{-4}$ ) as a proof of concept. In all cases, the devices were designed to meet the same specifications in the X-band. Moreover, the folded structures do not fundamentally modify the resonator  $Q$ -factor. An inline topology with a center frequency  $f_o = 9.45$  GHz, bandwidth  $BW = 200$  MHz ( $FBW = 2.11\%$ ), and size  $32.1 \times 7 \times 2$  mm was established as a reference for comparisons with other arrangements [see Fig. 12(a)]. This filter was modified to perform both the aforementioned transitions and inductive irises folded at  $90^\circ$ . Rounded corners ( $r_j = 1.7$  mm) were also realized to reduce the losses due to the high current density at the edges and avoid internal reflections [see Fig. 12(b)]. Four filter examples were optimized in HFSS [see Fig. 12(c)] to fulfill the original specifications and provide different features (Step ① in Fig. 2). EM simulations confirmed a negligible influence on the resonator  $Q$ -factor that compose the proposed folded filters described as follows.

- 1) *C-Shaped (Cs) Filter*: This approach implements a bending angle of  $90^\circ$  to the irises between resonators 1 and 2 and 3 and 4 to surround other associated components placed on the carrier board [red area in Fig. 13(a)]. These devices can be interconnected to the filter from both sides of the resonator thanks to the symmetry of the transition, thus enhancing the efficiency of the PCB area utilized. Moreover, the interconnection paths can be shortened to improve the system performance. The Cs filter could be also used as a reflector for EM fields or to isolate specific regions of the system. The inductive irises were placed at the base of the device to maximize the surface contact between the filter and the board, facilitate the part assembly, and ensure a good electrical connection.
- 2) *Bridge Filter*: The possibility to rotate the rectangular resonators while maintaining the same access configuration is exploited in this prototype. The Cs filter design was flipped to create a new version where interconnection lines could cross underneath and facilitate the PCB routing. Moreover, the area below the filter can

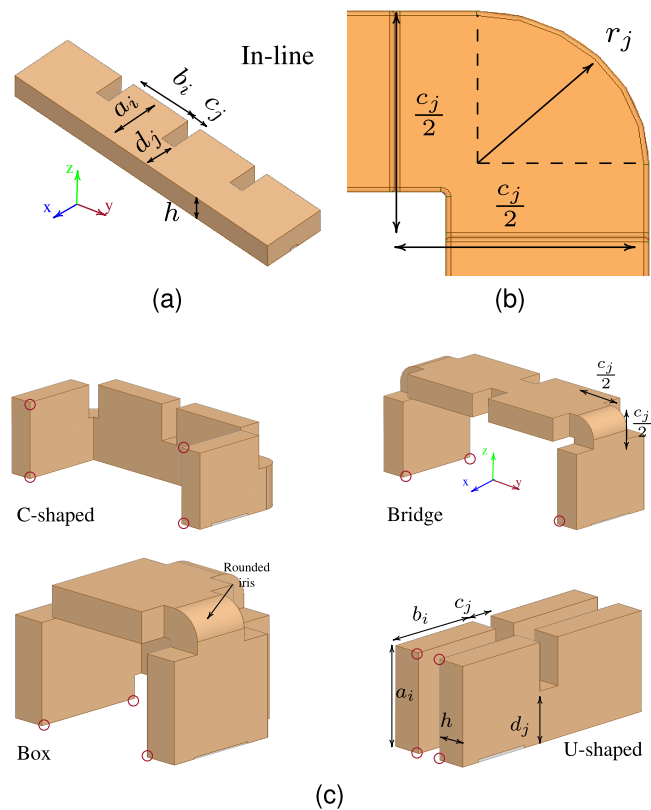


Fig. 12. (a) Reference inline filter. (b) Rounded iris. (c) Three-dimensional alumina filter designs: bridge, Cs, Us, and box. Support anchor points are highlighted in red.

be leveraged to place integrated circuits or microwave planar devices. Unlike the Cs filter, the irises were centered with respect to the resonators to balance the overall weight.

- 3) *Box Filter*: Structure folding was fully explored in this design. The box filter was developed as a first approach toward the implementation of heterogeneous integrated subsystems where other parts of the circuit can be interconnected from the inside [51] in a packaged fashion. Hence, the device can provide a dual functionality, as passive filter device and as part of the package itself. Another possible scenario could be the development of dual-band antenna arrays printed on ceramic blocks as suggested in [52]. Furthermore, this approach removes the inter-resonator connection constraints since nonadjacent resonators can be more easily linked, promoting the conception of diverse filter topologies.
- 4) *U-Shaped (Us) Filter*: Area reduction is fully exploited in this design. The Us filter was devised as a compact folded version of the C-shape and no other components can be embedded inside.

Fig. 12 and Table III show the dimensions of the suggested designs, where  $i = 1, 2, 3, 4$  represents the resonator number and  $j = 1, 2, 3$  the iris number. The substrate thickness  $h = 2$  mm, the access dimensions  $W_{acc} = 4$  mm and  $H_{acc} = 0.2$  mm are the same for all cases. The designs were conceived to let the resonators and irises faces exposed for the

TABLE III  
FILTER DESIGN DIMENSIONAL PARAMETERS

Dimension (mm)	Bridge	C-shaped	U-shaped	Box
$a_{1,2,3,4}$	6.998	6.998	6.998	6.966
$b_{1,4}$	6.396	6.453	6.679	6.866
$b_{2,3}$	6.704	7.007	7.249	6.492
$c_{1,3}$	5.000	5.000	1.566	5.000
$c_2$	3.527	1.639	1.804	5.000
$d_{1,3}$	2.997	3.922	3.600	3.469
$d_2$	1.639	3.614	3.750	3.274
$L_{acc}$	1.293	1.133	1.054	1.113

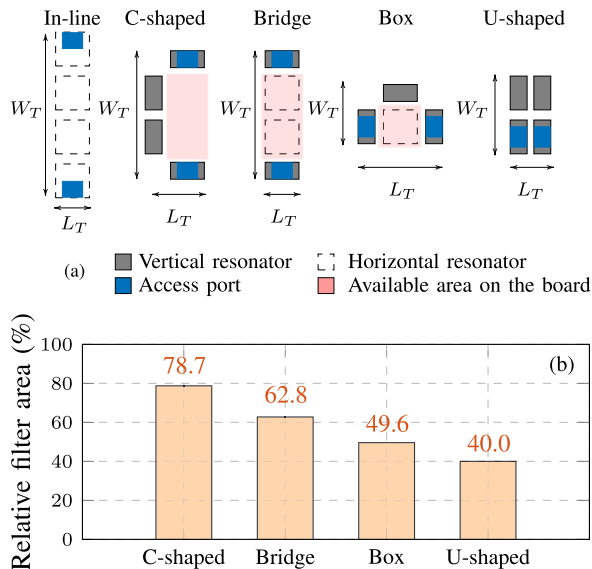


Fig. 13. (a) Three-dimensional printed filters footprint and (b) relative area ( $W_T \times L_T$ ) comparison with the inline reference filter.

post-fabrication tuning stage. The horizontally oriented resonators arrangement of some designs, such as in the box and bridge filters, is a convenient feature for automated assembly processes. Despite the access ports were intentionally placed in line to meet industry preferences, the structure bending at different angles allows other orientations better adapted to each front-end board layout. Fig. 13 illustrates the footprints of the four examples and their relative size reduction in comparison to the inline filter. The relative filter area was calculated as the ratio between the 3-D filters area ( $W_T \times L_T$ ) and the reference surface ( $233 \text{ mm}^2$ ). Furthermore, the available surface below and inside the bridge, box, and Cs filters can be leveraged to place other devices and make a better use of the board area.

### C. 3-D Printed Filters

The realization of prototypes such as the Box filter could be difficult to carry out with classical manufacturing methods. AM is an useful tool for the creation of complex-shape components. Nevertheless, the substrate hardening during the debinding and sintering steps are critical processes in ceramic SLA. Part of the accuracy can be lost due to the material shrinkage as a result of the solvents evaporation. Special care must be taken to elude pronounced deformations that could affect the part's dimensions and integrity [53].

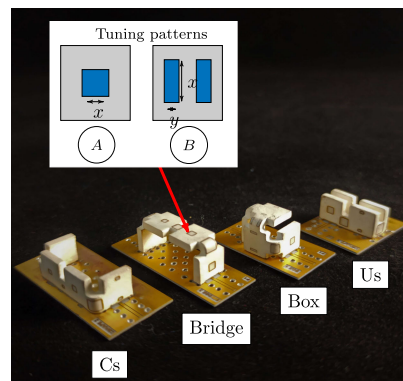


Fig. 14. Surface-mounted laser-tuned 3-D printed filters. (A) and (B) are the SS and 2-RS tuning patterns used for the DUTs S-parameters compensation.

Ceramic links were added between the specific joints highlighted in red in Fig. 12 to fix the structures and avoid deformations driven by the stress relief during the heat treatment. The supports were then removed once the process had been completed. The devices were printed prioritizing maximum flatness on the surface in contact with the board to ensure a correct assembly. The fabricated samples were measured with a digital microscope to characterize the size discrepancies. Results exhibit a dimension mismatch between  $-270 \mu\text{m} \leq \Delta x \leq 60 \mu\text{m}$ ,  $-280 \mu\text{m} \leq \Delta y \leq 170 \mu\text{m}$  and  $-200 \mu\text{m} \leq \Delta z \leq 256 \mu\text{m}$ . No particular differences were observed depending on the structure orientation (horizontally suspended or vertically placed) showing similar fabrication dispersion. The fabrication tolerance seems to be contained within the specified ranges regardless the printing position. Sharp corners and edges show a rounded fashion with a radius less than 0.2 mm. The devices were metal coated by means of an aerosol silver coating process [43] to enhance the  $Q$ -factor. Typical conductivity between  $20 \text{ S}/\mu\text{m} \leq \rho \leq 30 \text{ S}/\mu\text{m}$  can be achieved for a deposited layer of  $4 \mu\text{m}$  with this technique. Finally, the accesses were laser engraved to finalize the fabrication process. A mean weight of 1.39 g was measured in several samples of different filter designs. The devices were assembled into a RO4003C board (0.4 mm thick) with alignment patterns to facilitate the placement. Fig. 14 shows the manufactured filters and their assembly on the carrier substrate.

## VI. MEASUREMENTS AND LASER CORRECTION

The DUTs were measured with a ZVA 87 VNA connected to a  $500 \mu\text{m}$  pitch GSG probe tip. The data obtained throughout the measurement campaign confirmed a non-negligible dispersion of the filters response in every tested sample driven by SLA manufacturing imperfections. Prefabrication sensitivity analysis helped to estimate their impact and study the implementation of corrections. However, deformations and surface irregularities are difficult to foresee beforehand. Moreover, the reproduction of complex structural deformations observed in fabricated samples is hard to achieve in custom design models. Tuning strategies based on back-simulations cannot be accurately applied within this context. Otherwise, the method proposed in Section II suggests a convenient option to carry out the device tuning, given that the corrections are directly

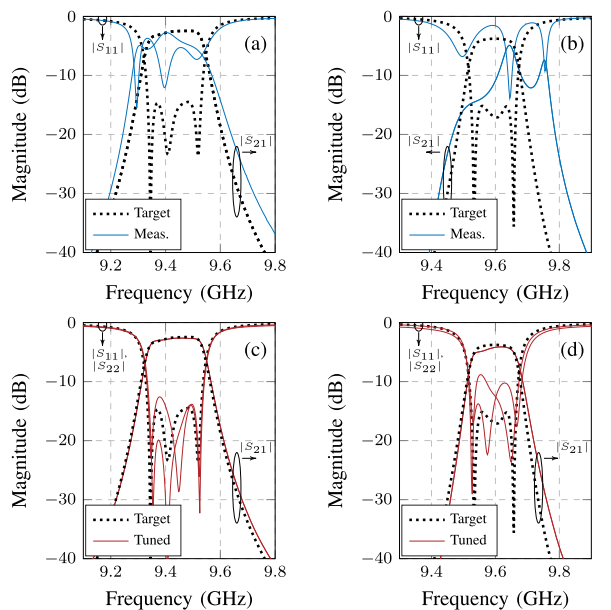


Fig. 15. Pretuned and post-tuned 3-D printed filters measured  $S$ -parameters: (a) and (c) Cs, and (b) and (d) Us.

performed using the measured  $S$ -parameters. Nevertheless, its capacity to compensate manufacturing imperfections greatly depends on the error magnitude to be corrected.

The less dispersive samples noticed among the four filter prototypes were the Cs and Us devices. Unlike the box and bridge filters, these designs present no hanging structures, thus reducing the risk of strong deformations. In some cases, the measured samples showed one or more poles shifted out-of-band from the target frequency (EM initial filter in Fig. 2). The quality factor degradation and inaccuracy driven by the high correction required to relocate the poles toward the target would be unacceptable. For that reason, the filters were re-centered to an intermediate target frequency within the tuning range to test the correction in every prototype. The target center frequency in each case was:  $f_{0\text{Bridge}} = 9.55$  GHz,  $f_{0\text{Cs}} = 9.45$  GHz, and  $f_{0\text{Box}} = f_{0\text{Us}} = 9.6$  GHz. The tuning patterns presented in Section IV were adopted to correct the fully 3-D printed filters in both irises and resonators (see Fig. 14).

Fig. 15 depicts the pre- and post-tuning measured  $S$ -parameters of the Cs and Us filters. On the one hand, results reveal a good agreement between the target and tuned filter response in the Cs sample as a result of the tuning methodology in only one loop. The filter shows post-tuning insertion losses between 2 and 3 dB within the passband and return loss better than 12.65 dB [see Fig. 15(c)]. On the other hand, the inter-resonator coupling factors extracted from the Us filter CM show a good match with the target matrix and an important improvement of  $\Delta f_0$  in every resonator. Effectively, considering the starting frequency response [see Fig. 15(b)], the effect of the tuning procedure shows a clear enhancement in the filter  $S$ -parameters [see Fig. 15(d)]. A second tuning loop could be applied to finely tune the filter response. However, the correction risks to degrade the quality factor to impractical values.

TABLE IV  
POST-TUNING MEASURED FILTERS PARAMETERS

Parameter	Bridge	C-shaped	U-shaped	Box
Center freq. (GHz)	9.567	9.455	9.598	9.596
Bandwidth (MHz)	135	200	164	190
Return Loss (dB)	8.02	12.65	8.82	3.39
Insertion Loss (dB)	5.00	2.64	4.89	5.62
Quality factor (Qo) *	N/A	550	330	N/A
Flatness (dB)	0.34	0.29	0.78	3.32

\* Effective quality factor estimated from an equivalent 4th order Chebyshev band-pass filter with the same  $f_0$  and bandwidth.

In the remaining prototypes, the initial filter response is highly dispersive as a result of the structural deformations, therefore, the error to be compensated is quite elevated. The tuning process manages to re-center the filters and greatly enhance the overall response. Nonetheless, the final results achieved are not as accurate and symmetric as in the other designs, and the  $Q$ -factor cannot be fairly extracted for comparison in these cases. Table IV summarizes the measured parameters for all the designs after the tuning stage. The  $Q$ -factors estimated from the measured results suggests that the tuning patterns add extra losses. As expected from the study conducted in Section III, the filters that require a higher degree of corrections exhibit greater  $Q$ -factor degradation.

## VII. DISCUSSION

To the best of the author's knowledge, most of the examples found in the bibliography related to 3-D SMT ceramic filters are focused on 2.5-D monoblock components placed horizontally on the carrier board. Three-dimensional printing techniques can lead to the exploration of complex-shape ceramic objects and their integration with heterogeneous technologies for the development of multifunction devices. However, the current manufacturing tolerance of ceramic SLA process is a limiting factor for the implementation of microwave devices. The structure complexity of the object, in addition to the maximum operating frequency needed, hinders the successful application of this approach, especially above sub-6 GHz bands. Previous experiments conducted by our group reported unacceptable results of 3-D printed millimeter-wave BPF as a direct consequence of these observations. The return of experience confirmed that a reliable post-fabrication method was mandatory to enable the implementation of such devices. The tuning approach developed was mainly inspired by similar laser engraving techniques and applied to our particular case for the correction of monolithic dielectric-filled cavity filters. The validation of the method was first realized using simpler standard inline designs to corroborate the expected functioning of the tuning patterns. The experiments were also important to test the process flow as well as the semiautomated tuning setup and measurement testbench. The corrected devices exhibited a filter response close to the expected specifications, demonstrating a good agreement between the target frequency response and measurements after the post-fabrication tuning process. Despite the method being irreversible, the tuning patterns can be also combined throughout the several tuning loops to finely tune the device and achieve the desired specifications.

However, it should be considered that this procedure aggregates extra radiating losses to the device. High corrections are equivalent to high losses and a non-negligible reduction of the  $Q$ -factor. Furthermore, over-etching and samples misalignment can add an extra source of error, leading to small correction differences and avoiding achieving the exact simulated result. Nonetheless, the current setup can be easily fully automated to minimize the user manipulation. Automated steps can include: autonomous probe station measurements; verification of the device tuning suitability from the initial filter conditions; determination of the required patterns and size optimization in every part of the structure; generation of CAD pattern files for the laser machine; and automatic re-optimization of complementary tuning patterns. The fully automated setup could then autonomously tune a batch of filters and release the samples once the needed correction has been applied, avoiding redesigning the prototype and reducing manufacturing costs and time.

The validation of the aforementioned procedure enables the exploration of more complex structures designed to fulfill the RF front-end scenarios suggested in Fig. 1. The four fully 3-D printed ceramic BPF prototypes described in Section V provide valuable information for the first realizations of these scenarios. The vertically-oriented cavity resonator filters can be used by the designer to adapt the component to the board floor-planning requirements and simplify the layout. They can also be leveraged to surround or contain other circuit elements, integrate more functionalities in the same space, and enhance the EM isolation of specific regions of the system. Moreover, since in  $TE_{101}$  mode the quality factor increases with the resonator thickness ( $h_i$ ), a wider resonator base gives more stability to the device, enhances the ground contact to the board, eases the welding procedure, and improves the filter performances.

The addition of ceramic supports during the fabrication can help to reduce other sources of errors such as high deformations, cracks, and the collapse of overhanging structures. Nevertheless, these defects are hard to predict and model during the design step. Sensitivity analysis performed during the design stage confirmed that even taking these precautions, a post-fabrication step is needed to correct the frequency response of the filters. The printing orientation was chosen to prioritize a flat surface in the area in contact with the substrate. However, this decision imposes an inevitable trade-off between the SMT transition and the structural deformations that could be reduced with the selection of other printing orientations.

The characterization of the manufactured samples by means of a laser scanner exhibited an average fabrication dispersion of  $\pm 280 \mu\text{m}$  and a maximum deviation of  $\pm 350 \mu\text{m}$ . No particular trend was noted depending on the orientation of the structures except for a tendency to smaller dimensions compared to the design in the  $x$ -/ $y$ -direction. This systematic error could be a product of an excessive shrinkage of the samples during the sintering step. Based on the extracted information, it is possible to update the manufacturing process and enhance the accuracy in future batches. The dispersion observed was rather homogeneous in every case.

## VIII. CONCLUSION

An approach toward the use of ceramic SLA processes for the conception of 3-D printed passive microwave BPFs and an associated post-fabrication tuning method was presented. 2.5-D and 3-D prototypes were designed and fabricated to identify the main milestones to overcome when developing modern communication devices for the scenarios described in Fig. 1.

The structural deformations observed during the digital reconstruction of the fabricated samples revealed the difficulties of accurately reproducing the real object in an EM simulation software environment. Therefore, the utilization of a tuning method based on the CM relative variations instead of purely back simulations seems to be a more appropriated choice in this case. The experimental results helped to validate the steps of the method proposed in Section II, and the capability of the rectangular and SS patterns to correct the frequency response of 3-D printed ceramic cavity filters. Post-tuning measurements showed an improvement of the filters' response and a good agreement between the target and one-loop tuned filters for those devices with lower initial error. Overall, those prototypes without hanging structures (2.5-D, Cs and Us) show less dispersion and deformations. A great filter response enhancement was noted in all the cases even though the final result was not optimal. Furthermore, the experience obtained from the 3-D laser correction applied to the rounded irises implemented in this work suggests that the surface etching can be carried out without major difficulties. Other iris structures can be studied in future designs to reduce the engraving complexity of tuning patterns.

The symmetric magnetic field distribution of the  $TE_{101}$  rectangular cavity resonators utilized in the fully 3-D printed designs proposed helped to the development of a SMT transition compliant to industrial pick and place misalignment tolerances. Vertically oriented resonators bring two main advantages: an important area reduction in comparison to traditional designs and a natural tendency to build the structure in volume. However, these transitions cannot be tuned to modify the external coupling. Future efforts will contemplate the inclusion of tuning ports capabilities and the development of integrated subsystems in those prototypes that exhibit better results. The investigation of other printing strategies can help to reduce the deformations of the most complex devices and minimize the required corrections. Other passive devices such as waveguides, diplexers, or power splitters could be designed using the same approach.

## REFERENCES

- [1] R. Bahr, B. Tehrani, and M. M. Tentzeris, "Exploring 3-D printing for new applications: Novel inkjet- and 3-D-printed millimeter-wave components, interconnects, and systems," *IEEE Microw. Mag.*, vol. 19, no. 1, pp. 57–66, Jan. 2018.
- [2] *Wohlers Annual Report: Additive Manufacturing and 3D Printing State of the Industry*, Wohlers Associates, Washington, DC, USA, 2021.
- [3] W. Hong et al., "Multibeam antenna technologies for 5G wireless communications," *IEEE Trans. Antennas Propag.*, vol. 65, no. 12, pp. 6231–6249, Dec. 2017.

- [4] S. Shinjo, K. Nakatani, K. Tsutsumi, and H. Nakamizo, "Integrating the front end: A highly integrated RF front end for high-SHF wide-band massive MIMO in 5G," *IEEE Microw. Mag.*, vol. 18, no. 5, pp. 31–40, Jul. 2017.
- [5] L. Chettri and R. Bera, "A comprehensive survey on Internet of Things (IoT) toward 5G wireless systems," *IEEE Internet Things J.*, vol. 7, no. 1, pp. 16–32, Jan. 2020.
- [6] A. Eid et al., "Inkjet-/3D-/4D-printed perpetual electronics and modules: RF and mm-Wave devices for 5G+, IoT, smart agriculture, and smart cities applications," *IEEE Microwave Magazine*, vol. 21, no. 12, pp. 87–103, Dec. 2020.
- [7] F. Babich, M. Comisso, A. Cuttin, M. Marchese, and F. Patrone, "Nanosatellite-5G integration in the millimeter wave domain: A full top-down approach," *IEEE Trans. Mobile Comput.*, vol. 19, no. 2, pp. 390–404, Feb. 2020.
- [8] J. Ma, "The design-for-cost of millimeter-wave front-end for 5G and beyond," in *Proc. IEEE Int. Conf. Commun. China*, Chongqing, China, Aug. 2020, pp. 395–400.
- [9] R. Sorrentino and O. A. Peverini, "Additive manufacturing: A key enabling technology for next-generation microwave and millimeter-wave systems [point of view]," *Proc. IEEE*, vol. 104, no. 7, pp. 1362–1366, Jul. 2016.
- [10] R. Sorrentino, P. Martin-Iglesias, O. A. Peverini, and T. M. Weller, "Additive manufacturing of radio-frequency components [scanning the issue]," in *Proc. IEEE*, vol. 105, no. 4, pp. 589–592, Apr. 2017.
- [11] Y. Dia, L. Huitema, S. Bila, M. Thevenot, N. Delhote, and C. Delavaud, "3D compact high-Q filter made of high-permittivity ceramic," in *Proc. 49th Eur. Microw. Conf. (EuMC)*, Oct. 2019, pp. 304–307.
- [12] G. Addamo et al., "Electromagnetic and mechanical analyses of a 3D-printed Ka-band integrated twist and orthomode transducer," in *IEEE MTT-S Int. Microw. Symp. Dig.*, Bochum, Germany, Jul. 2019, pp. 31–33.
- [13] E. Laplanche et al., "A Ku-band diplexer based on 3 db directional couplers made by plastic additive manufacturing," in *Proc. Eur. Microw. Conf.*, Nuremberg, Germany, 2017, pp. 428–431.
- [14] G. Addamo et al., "3-D printing of high-performance feed horns from Ku-to V-bands," *IEEE Antennas Wireless Propag. Lett.*, vol. 17, no. 11, pp. 2036–2040, Nov. 2018.
- [15] P. Martin-Iglesias, M. van der Vorst, J. Gumpinger, and T. Ghidini, "Esa's recent developments in the field of 3D-printed RF/microwave hardware," in *Proc. Eur. Conf. Antennas Propag.*, Paris, France, 2017, pp. 553–557.
- [16] E. Laplanche et al., "Additive manufacturing of low cost and efficient proof of concepts for microwave passive components," *IET Microw. Antennas Propag.*, vol. 11, no. 14, pp. 1997–2004, Nov. 2017.
- [17] A. Syed Nauroze et al., "Additively manufactured RF components and modules: Toward empowering the birth of cost-efficient dense and ubiquitous IoT implementations," *Proc. IEEE*, vol. 105, no. 4, pp. 702–722, Apr. 2017.
- [18] A. Delage et al., "Aerosol jet printing of millimeter wave transmission lines on 3D ceramic substrates made by additive manufacturing," in *IEEE MTT-S Int. Microw. Symp. Dig.*, Philadelphia, PA, USA, Jun. 2018, pp. 1557–1560.
- [19] B. K. Tehrani, R. A. Bahr, W. Su, B. S. Cook, and M. M. Tentzeris, "E-band characterization of 3D-printed dielectrics for fully-printed millimeter-wave wireless system packaging," in *IEEE MTT-S Int. Microw. Symp. Dig.*, Honolulu, HI, USA, Jun. 2017, pp. 1756–1759.
- [20] R. Bahr, B. Teharani, M. Tentzeris, and K. Byers, "A novel integration of stereolithography and inkjet printing for multichip modules with high frequency packaging applications," in *Proc. IEEE 68th Electron. Compon. Technol. Conf. (ECTC)*, San Diego, CA, USA, May 2018, pp. 2498–2504.
- [21] X. Wang, K.-L. Wu, and W.-Y. Yin, "A novel surface-mounted monoblock dielectric filter," *IEEE Trans. Compon., Packag., Manuf. Technol.*, vol. 4, no. 11, pp. 1822–1827, Nov. 2014.
- [22] C. Menudier et al., "Innovative materials and fabrication process to develop new RF components and concepts," in *Proc. 11th Eur. Conf. Antennas Propag. (EUCAP)*, Paris, France, Mar. 2017, pp. 594–597.
- [23] J. C. Fisher, *A Brief History of the Nd: YAG Laser*, S. N. Joffe and Y. Oguro, Eds. New York, NY, USA: Springer, 1988, doi: [10.1007/978-1-4612-3728-0\\_2](https://doi.org/10.1007/978-1-4612-3728-0_2).
- [24] P. Deluca, "A review of thirty-five years of laser trimming with a look to the future," *Proc. IEEE*, vol. 90, no. 10, pp. 1614–1619, Oct. 2002.
- [25] N. J. Parker, S. W. Goodyear, D. J. P. Ellis, and R. G. Humphreys, "Laser tuning of HTS microwave filters," *Phys. C, Supercond.*, vols. 372–376, pp. 519–522, Aug. 2002. [Online]. Available: <https://www.sciencedirect.com/science/article/pii/S0921453402007414>
- [26] A. H. Khalil et al., "3-D pyramidal and collective Ku band pass filters made in alumina by ceramic stereolithography," in *IEEE MTT-S Int. Microw. Symp. Dig.*, Baltimore, MD, USA, Jun. 2011, pp. 1–4.
- [27] M. Giordani and M. Zorzi, "Non-terrestrial networks in the 6G era: Challenges and opportunities," *IEEE Netw.*, vol. 35, no. 2, pp. 244–251, Mar. 2021.
- [28] H. Tataria, M. Shafi, A. F. Molisch, M. Dohler, H. Sjöland, and F. Tufvesson, "6G wireless systems: Vision, requirements, challenges, insights, and opportunities," *Proc. IEEE*, vol. 109, no. 7, pp. 1166–1199, Jul. 2021.
- [29] M. Boschiero, M. Giordani, M. Polese, and M. Zorzi, "Coverage analysis of UAVs in millimeter wave networks: A stochastic geometry approach," in *Proc. Int. Wireless Commun. Mobile Comput. (IWCMC)*, Limassol, Cyprus, Jun. 2020, pp. 351–357.
- [30] B. Yang, Z. Yu, J. Lan, R. Zhang, J. Zhou, and W. Hong, "Digital beamforming-based massive MIMO transceiver for 5G millimeter-wave communications," *IEEE Trans. Microw. Theory Techn.*, vol. 66, no. 7, pp. 3403–3418, Jul. 2018.
- [31] E. Laplanche et al., "Tunable filtering devices in satellite payloads: A review of recent advanced fabrication technologies and designs of tunable cavity filters and multiplexers using mechanical actuation," *IEEE Microw. Mag.*, vol. 21, no. 3, pp. 69–83, Mar. 2020.
- [32] P. Harscher, R. Vahldieck, and S. Amari, "A novel technique for automated post production filter tuning," in *Proc. APMC. Asia-Pacific Microw. Conf.*, Taipei, Taiwan, 2001, pp. 751–754.
- [33] Y. Zhang, H. Meng, and K.-L. Wu, "A hybrid genetic algorithm for robot automatic tuning of microwave filters," in *IEEE MTT-S Int. Microw. Symp. Dig.*, Shanghai, China, Jun. 2020, pp. 1–3.
- [34] A. Dia, C. Duroseau, C. Menudier, L. Carpentier, O. Ruatta, and S. Bila, "Gradient descent shape optimization of microwave circuits using bézier curves parametrization," in *Proc. Eur. Microw. Conf.*, Madrid, Spain, 2018, pp. 158–161.
- [35] C. Kwak, M. Uhm, I. Yom, and H. J. Eom, "Automated microwave filter tuning using curve similarity and weighted least squares," *IEEE Microw. Wireless Compon. Lett.*, vol. 22, no. 10, pp. 539–541, Oct. 2012.
- [36] Y. Marchives, N. Delhote, S. Verdeyme, and P. M. Iglesias, "Wide-band dielectric filter at C-band manufactured by stereolithography," in *Proc. 44th Eur. Microw. Conf.*, Rome, Italy, Oct. 2014, pp. 187–190.
- [37] A. El Mostrah, B. Potelon, E. Rius, C. Quendo, J. F. Favennec, and H. Leblond, "Association of HPWRs and DBRs for a high rejection C-band filter with post-tuning elements," *IEEE Microw. Wireless Compon. Lett.*, vol. 23, no. 6, pp. 297–299, Jun. 2013.
- [38] Y. Chen, Y. Zhang, and K.-L. Wu, "A dual-mode monoblock dielectric bandpass filter using dissimilar fundamental modes," *IEEE Trans. Microw. Theory Techn.*, vol. 69, no. 8, pp. 3811–3819, Aug. 2021.
- [39] S. Courreges, C. Thibon, F. A. Houndonougbo, A. Crunteanu, V. Madrangeas, and M. Maignan, "Tuning of superconducting filters with laser ablation technique," *IEEE Trans. Appl. Supercond.*, vol. 19, no. 5, pp. 3715–3721, Oct. 2009.
- [40] A. E. Atia and A. E. Williams, "Narrow-bandpass waveguide filters," *IEEE Trans. Microw. Theory Techn.*, vol. MTT-20, no. 4, pp. 258–265, Apr. 1972.
- [41] P. Aurelien, V. Serge, D. Nicolas, B. Stephane, T. Olivier, and L. Carpentier, "Continuously tunable X-band filter using a 3D spiral ribbon," in *IEEE MTT-S Int. Microw. Symp. Dig.*, Reykjavik, Iceland, Aug. 2018, pp. 1–4.
- [42] N. Delhote, D. Baillargeat, S. Verdeyme, C. Delage, and C. Chaput, "Ceramic layer-by-layer stereolithography for the manufacturing of 3-D millimeter-wave filters," *IEEE Trans. Microw. Theory Techn.*, vol. 55, no. 3, pp. 548–554, Mar. 2007.
- [43] W. Feuray et al., "Evaluation of metal coating techniques up to 66 GHz and their application to additively manufactured bandpass filters," in *Proc. Eur. Microw. Conf.*, Nuremberg, Germany, 2017, pp. 512–515.
- [44] F. Ren, W. Hong, and K. Wu, "Design and implementation of an SIW triple-mode filter," in *Proc. 3rd Asia-Pacific Conf. Antennas Propag.*, Harbin, China, Jul. 2014, pp. 1228–1230.
- [45] M. S. M. Mollaei, R. Heydarian, E. Zanganeh, and S. H. Sedighy, "Triple-bands Ka-band frequency selective surface filter with different polarized transmitting performance in each band," in *Proc. Eur. Conf. Antennas Propag.*, Krakow, Poland, 2019, pp. 1–3.
- [46] L. Yan, W. Hong, G. Hua, J. Chen, K. Wu, and T. J. Cui, "Simulation and experiment on SIW slot array antennas," *IEEE Microw. Wireless Compon. Lett.*, vol. 14, no. 9, pp. 446–448, Sep. 2004.
- [47] A. Srivastava, R. K. Chaudhary, A. Biswas, and M. Jaleel Akhtar, "Dual-band L-shaped SIW slot antenna," in *Proc. Int. Conf. Microw. Photon.*, Dhanbad, India, 2013, pp. 1–3.

- [48] J.-S. Hong and M. J. Lancaster, *Microstrip Filters for RF/Microwave Applications*. New York, NY, USA: Wiley, 2001.
- [49] R. J. Cameron, C. M. Kudsia, and R. R. Mansour, *Microwave Filters for Communication Systems: Fundamentals, Design and Applications*. New York, NY, USA: Wiley, 2018.
- [50] K. Onaka et al., "28 GHz wideband filter using quartz crystal waveguide for massive MIMO antenna unit," in *IEEE MTT-S Int. Microw. Symp. Dig.*, Honolulu, HI, USA, Jun. 2017, pp. 1468–1471.
- [51] J. Kimionis, A. Georgiadis, M. Isakov, H. J. Qi, and M. M. Tentzeris, "3D/inkjet-printed origami antennas for multi-direction RF harvesting," in *IEEE MTT-S Intern. Microw. Symp.*, Phoenix, AZ, USA, May 2015, pp. 1–4.
- [52] S. Wu, A. Zhao, and Z. Ren, "Design of dual-band millimeter-wave antenna array for 5G communication system," in *Proc. Intern. Symp. Antennas Propag.*, Busan, South Korea, 2018, pp. 1–2.
- [53] H. Khalil et al., "Advanced design and manufacturing of microwave components based on shape optimization and ceramic stereolithography process," in *IEEE MTT-S Int. Microw. Symp. Dig.*, Chengdu, China, Dec. 2008, pp. 15–18.



**Andrés Fontana** (Member, IEEE) received the Ph.D. degree in high-frequency electronics from the University of Limoges, Limoges, France, in 2022.

He is currently a Post-Doctoral Researcher with the Advanced RF Technologies (ART) Group, Tyn-dall National Institute, Cork, Ireland. His research interests include RF active and passive devices and subsystems, monolithic microwave integrated circuit (MMIC) design, additive manufacturing, and heterogeneous integration technologies for wireless communication applications.



**Anthony Delage** received the Ph.D. degree from the University of Limoges, Limoges, France, in 2019.

Then, he joined ARIANEGROUP, Le Haillan, France, where he is specialized in antennas for space and military applications. His current topics of interest include antenna design and 3-D printed manufacturing.



**Aurélien Périgaud** (Member, IEEE) was born in Limoges, France, in 1981. He received the Ph.D. degree from the University of Limoges, Limoges, in 2009.

He is currently a Research Engineer with the XLIM Research Institute, University of Limoges. His research activities are mainly dedicated to the packaging of millimeter-wave modules, to the design of original resonators and filters, and tunable versions of such devices.



**Patrice Richard** received the degree in engineering from the Institut Supérieur d'Electronique du Nord (ISEN), Lille, France, in 1995.

He started his career at THALES, Toulouse, France, in 1995, as a Research and Development Engineer. Since 2008, he has been working as a Radio Architect and is now focused on the expertise of hardware platforms.



**David Carsenat** received the Ph.D. degree in microwave electronic from the University of Limoges, Limoges, France, in 2003.

From 2003 to 2015, he worked as an Assistant Professor with the XLIM Laboratory, CNRS/University of Limoges. Since 2015, he has been working with Thales SIX, Brive-la-Gaillarde, France, as a Radio Engineer for radio navigation systems.



**Guillaume Acikalin** received the master's degree in architecture and design on integrated systems from the University of Paris 6, Pierre and Marie Curie, Paris, France, in 2006.

Since 2006, he has been working with Thales SIX, Brive-la-Gaillarde, France, successively as a Software Engineer, the Software Engineering Manager, and then the Technical Product Manager for airborne radio products.



**Serge Verdeyme** was born in Meilhards, France, in June 1963. He is currently a Full Professor with the University of Limoges, Limoges, France.

He was the Vice-President of the University of Limoges from 2010 to 2021, where he conducts his research activities at the XLIM Research Laboratory, in the field of numerical modeling, optimization of microwave components and circuits, with a particular experience in the design of microwave filters, and multiplexers. He has been a Supervisor of 39 Ph.D. students. He has coauthored four book chapters,

73 articles in international refereed journals, and more than 150 international conference papers.



**Barbara Bonnet** received the M.Sc. degree in electrical engineering from ENSEEIHT, Toulouse, France, in 2007, and the M.Sc. degree in nanoscale science and technology from the Chalmers University of Technology, Gothenburg, Sweden, in 2007.

Since 2007, she has been working with the Microwave Department, Thales Alenia Space, Toulouse, first as a Technology Research and Development Engineer and since 2019 has been the Head of the Microwave Functions and Packaging Team.



**Ludovic Carpentier** received the Ph.D. degree in electrical engineering from the University of Limoges, Limoges, France, in 2012.

From 2012 to 2022, he was a Research and Development Engineer with the French Space Agency (CNES), Toulouse, France, where he was involved in microwave passive components area.



**Nicolas Delhote** (Member, IEEE) received the Ph.D. degree from the University of Limoges, Limoges, France, in 2007.

He has been with the XLIM Research Institute, University of Limoges, since 2007. He specializes in 3-D manufacturing technologies to fabricate RF and millimeter wave passive components (filters, waveguides, and RF transitions) and tunable variants. He has particularly focused most of his activities on additive manufacturing technologies and advanced materials for high-end applications (space

telecommunications, airborne radar applications, and high-frequency wireless telecommunications). He has been the Head of the Macao Research Group since 2016 (six permanent members, 11 Ph.D. students, and postdoctoral researchers).